International Journal of Bioprinting

RESEARCH ARTICLE

An integrated *in silico–in vitro* approach for bioprinting core–shell bioarchitectures

Supplementary File

S1. Material combinations and properties for the *in silico* simulations

The material combinations implemented in the computational model are listed in **Table S1**. For the shell composition, different concentrations of alginate were considered, ranging from 10 to 50 mg/mL. For the core, different materials were considered to model air, liquid, or solid cores. In the case of the liquid core, water and Pluronic solutions at 1 and 10 mg/mL were investigated, while for the solid core, the same shell concentrations of alginate were considered.

Different flow rates for core and shell were combined in a range from 10 to 50 μL/s, while the concentration of $CaCl_2$ solution was set to 0.1 M. The crosslinking time varied between 5 and 30 min.

Table S1. Material combinations investigated in the computational simulations

	Core material					
Shell material	**Solid**			**Liquid**		
Alginate [mg/mL]	10	Alginate [mg/mL]		10	Water	1–10 mg/mL Pluronic
	20			20		
	30			30		
	40			40		
	50			50		

S2. Force balance for drop formation estimation

We first estimated initial values for extruded droplet core and shell radii (respectively R_c^* and R_s) considering the equilibrium of forces during formation. These values served to generate an initial domain in the finite element method (FEM) models. Navier–Stokes equations for incompressible Newtonian fluids were implemented in cylindrical coordinates for the derivation of viscous (F_v) forces. The velocity profiles for core (v_c) and shell (v_s) considered in Equations SI and SII were also derived similarly, resulting in a parabolic (Poiseuille) profile, i.e., zero velocity at the walls (no slip boundary condition) and maximum at the center of the tube.

Then, the R_c^* and R_s were estimated by solving the balance between viscous (F_v), inertial (F_i), and surface tension (F_γ) forces for both the core (Equation S-I) and the shell (Equation S-II), as shown in **Figure S1**.

$$\begin{cases} F_{i-c} = \left(\rho_c g L + \rho_c \dfrac{v_c^2}{2}\right)\pi R_c^{*2} \\ F_{v-c} = 2\pi L \mu_c R_c^* \dfrac{dv_c}{dR} \\ F_{\gamma-c} = 2\pi\gamma_c R_c^* \cos\theta_c \\ v_c = \dfrac{2Q_c}{\pi R_{in}^2}\left(1-\left(\dfrac{R_c^*}{R_{in}}\right)^2\right) \end{cases} \rightarrow R_c^* = \frac{F_{i-c}+F_{v-c}+F_{\gamma-c}}{\frac{4}{3}\pi\rho_c g} \quad \text{(S-I)}$$

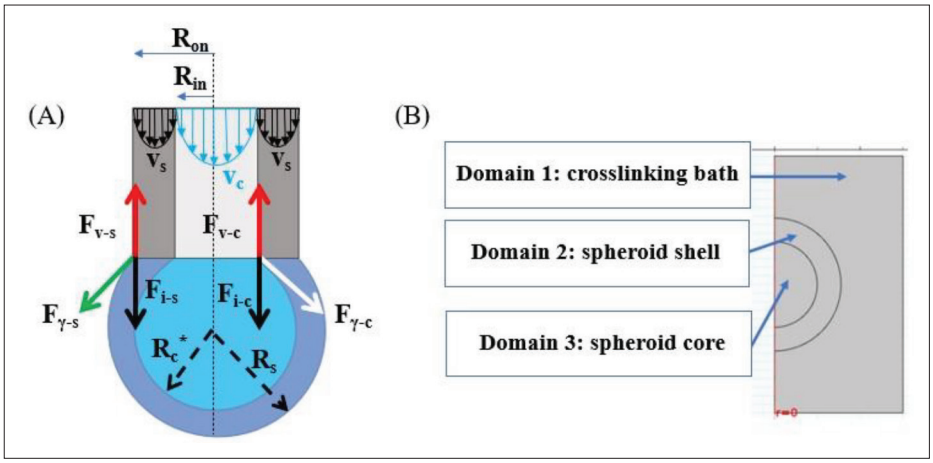

Figure S1. (A) Schematic of the force balance during the core–shell drop formation showing the different forces considered. The subscripts refer to the forces (i, inertial; v, viscous; g, surface tension) and to the region in which they act (s, shell; c, core). (B) FEM model domains in 2D-axial symmetric geometry.

$$\begin{cases} F_{i-s} = \left(\rho_s g L + \rho_s \dfrac{v_s^2}{2}\right)\pi R_s^2 \\ F_{v-s} = 2\pi L \mu_s R_s \dfrac{dv_s}{dR} \\ F_{\gamma-s} = 2\pi \gamma_s R_s \cos\theta_s \\ v_s = \dfrac{2Q_s}{\pi R_{on}^2}\left\{\left[\left(\dfrac{R_s}{R_{on}}\right)^2 - 1\right] + \left(1 - \left(\dfrac{R_{in}}{R_{on}}\right)^2\right)\dfrac{\ln\left(\dfrac{R_{on}}{R_s}\right)}{\ln\left(\dfrac{R_{in}}{R_{on}}\right)}\right\} \end{cases} \rightarrow R_s = \frac{F_{i-s} + F_{v-s} + F_{\gamma-s}}{\frac{4}{3}\pi\rho_s g} - \frac{\rho_c}{\rho_s} R_c^* \quad \text{(S-II)}$$

R_{in} and R_{on} indicate, respectively, the inner (R_{in} = i.d./2) and the outer (R_{on} = o.d./2) radii of the needle. Experimental contact angles (θ) and air–liquid surface tension (γ_s) were measured with a tensiometer using the pendant drop test (Optics Theta Lite, Biolin Scientific, Sweden) (**Table S2**), while the liquid–liquid interstitial tension γ_s was analytically estimated from the experimental core–shell data (**Table S3**). In addition, the experimental viscosity values (**Table S2**) were used to derive the relationship between the alginate solution viscosity and its concentration using the Curve Fitting tool in Matlab2022a. Solution viscosity at concentrations greater than 20 mg/mL, used in the computational models, was extrapolated on the base of the experimental curves.

Table S2. Experimental viscosity (shear rate $1.3 \times 10^3\ s^{-1}$) and air/liquid surface tension values

	Viscosity [mPa*s] at 37°C	Air–liquid surface tension [mN/m]
10 mg/mL alginate	53.20 ± 0.2	53.29 ± 3.13
20 mg/mL alginate	243.20 ± 0.3	60.17 ± 3.05
1 mg/mL Pluronic	4.25 ± 0.01	48.58 ± 4.06
10 mg/mL Pluronic	5.36 ± 0.05	41.66 ± 3.97
Water	0.72[1]	72.8[2]

Table S3. Interfacial tension between core–shell materials, estimated from the computational model

	Interfacial tension [N/m]	
	10 mg/mL alginate	**20 mg/mL alginate**
1 mg/mL Pluronic	$4.50 \times 10^{-3} \pm 2.36 \times 10^{-4}$	$2.50 \times 10^{-3} \pm 2.36 \times 10^{-4}$
10 mg/mL Pluronic	$6.17 \times 10^{-3} \pm 1.18 \times 10^{-3}$	$3.60 \times 10^{-3} \pm 1.98 \times 10^{-3}$
Air	$53.30 \times 10^{-3} \pm 3.12 \times 10^{-3}$	$60.20 \times 10^{-3} \pm 3.05 \times 10^{-3}$

S3. Estimated FEM model parameters

To describe the hindered diffusion coefficient in a matrix, the permeability κ needs to be considered to include the influence of the matrix structural properties. Therefore, to account for the hydrodynamic interaction between matrix fibers and diffusing macromolecules, the "effective medium" equation of Brinkman (Equation S-III)[3] was proposed. This equation describes macromolecule flux in a continuous phase, and it allows setting no-slip conditions at the surface of the alginate[4].

$$D' = \left\{ 1 + \left(\frac{R_H^{\,2}}{\kappa(\alpha)} \right)^{\frac{1}{2}} + \frac{1}{3}\left(\frac{R_H^{\,2}}{\kappa(\alpha)} \right) \right\}^{-1} \cdot D_0 = b \cdot D_0 \tag{S-III}$$

The coefficient b was estimated by combining the Brinkmann and Carman–Kozeny equations. In particular, the gel is considered a network of overlapping and crosslinked chains, and the characteristic descriptive parameter is the porosity $\in$, evaluated as $1 - \alpha(t)$. The chains forming the gel are treated as fixed obstacles that hinder the flux of macromolecules.

The Carman–Kozeny equation (Equation S-IV)[3] describes the permeability as a function of the hydrogel porosity $\in$ and the mean hydraulic radius of the species.

$$\kappa(\alpha) = \frac{\epsilon(\alpha) R_H^2}{k} \tag{S-IV}$$

k is the Kozeny factor (V), and it depends on channel shape and tortuosity: it increases with the porosity and can be evaluated considering the parallel and the normal components with respect to the flow coordinates.

$$\begin{cases} k_{\parallel} = 2\epsilon(\alpha)^3 / \left\{ (1-\epsilon(\alpha)) \left[\ln\left(\frac{1}{1-\epsilon(\alpha)} \right) - 3 + 4(1-\epsilon(\alpha)) - (1-\epsilon(\alpha))^2 \right] \right\} \\ k_{\perp} = 2\epsilon(\alpha)^3 / \left\{ (1-\epsilon(\alpha)) \left[\ln\left(\frac{1}{1-\epsilon(\alpha)} \right) - \frac{1-(1-\epsilon(\alpha))^2}{1+(1-\epsilon(\alpha))^2} \right] \right\} \end{cases} \rightarrow k = (2k_{\perp} + k_{\parallel})/3 \tag{S-V}$$

In **Table S4**, the Brinkmann factor b of different combinations of core–shell materials is reported, using the respective hydrodynamic radius and material properties.

Table S4. Brinkmann factor b in the shell for different core–shell material combinations after 15-min crosslinking

	Solid core—alginate	**Liquid core—1 mg/mL Pluronic**	**Liquid core—10 mg/mL Pluronic**
10 mg/mL alginate shell	0.281	0.341	0.327
20 mg/mL alginate shell	0.334	0.354	0.363

Table S5. Characteristic diffusion time of molecules in the alginate matrix and free medium considering the apparent diffusion coefficient after 15 min of crosslinking

Molecule	Diffusion time in the alginate matrix [s]	Diffusion time in free medium [s]
Ca^{2+}	5.31×10^3	1.73×10^3
Pluronic	1.86×10^5	6.86×10^3
Free alginate	1.57×10^8	1.17×10^6

Table S6. Model parameters for the evaluation of the apparent diffusion coefficient

Parameter		Symbol	Value	SI unit	Ref.
Hydrodynamic radius	Alginate	$R_{H_{alg}}$	200×10^{-9}	[m]	[5]
	Pluronic	$R_{H_{Plu}}$	1.170×10^{-9}	[m]	[6]
	Calcium ions	$R_{H_{CaCl_2}}$	0.296×10^{-9}	[m]	[7]
Diffusion coefficient ratio before and after gelling		δ	0.5	[-]	[8]
Gelation rate model parameter		n	5	[-]	[8]
Gelation degree for solid-like transition		α^*	0.2	[-]	[9]

S4. Adaptive mesh refinement and time-dependent numerical algorithm in Comsol Multiphysics 6

To improve the prediction of the outer contour of the alginate constructs, the adaptive mesh refinement routine was performed in Comsol Multiphysics 6 to identify the optimal mesh structure that provides the balance between mesh accuracy and computational time (**Figure S2**). In particular, the solution was first computed on an initial mesh (free tetrahedral fine elements, physic-controlled, **Figure S2A**). After estimating the regions where the computational error of the solution is higher than an absolute tolerance of 0.1, the geometry was re-meshed with finer tetrahedral elements in these regions and the model re-solved on the new mesh. The optimized mesh (**Figure S2B**) was obtained after 11 iterations of the mesh refinement algorithm.

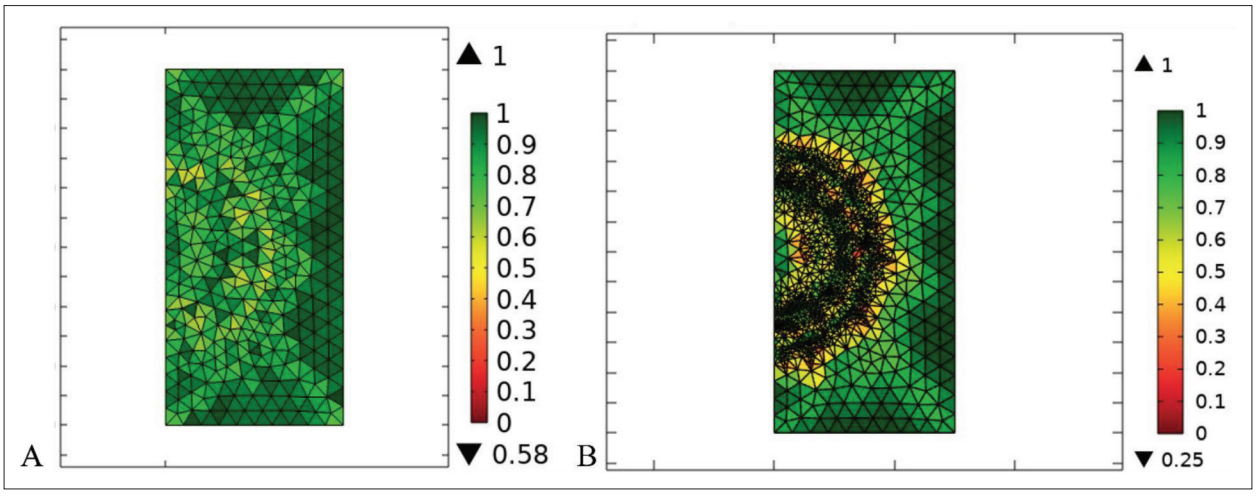

Figure S2. Mesh structure before (basic) (A) and after (B) the adaptive mesh refinement (scale bar: growth rate).

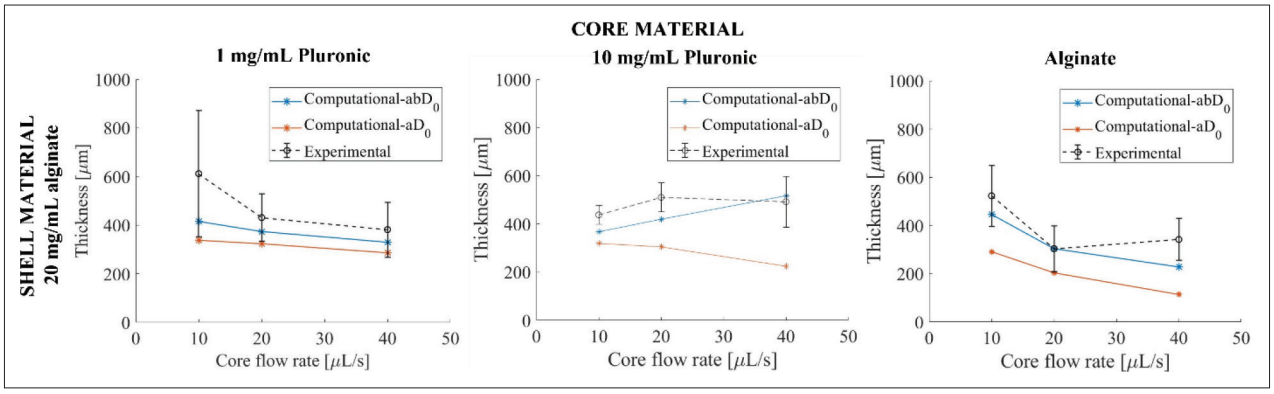

Figure S3. Comparison between the computational data obtained with and without the use of the Brinkmann correction and the experimental data in the case of core–shell construct with 20 mg/mL shell and different core composition obtained with needle 2.

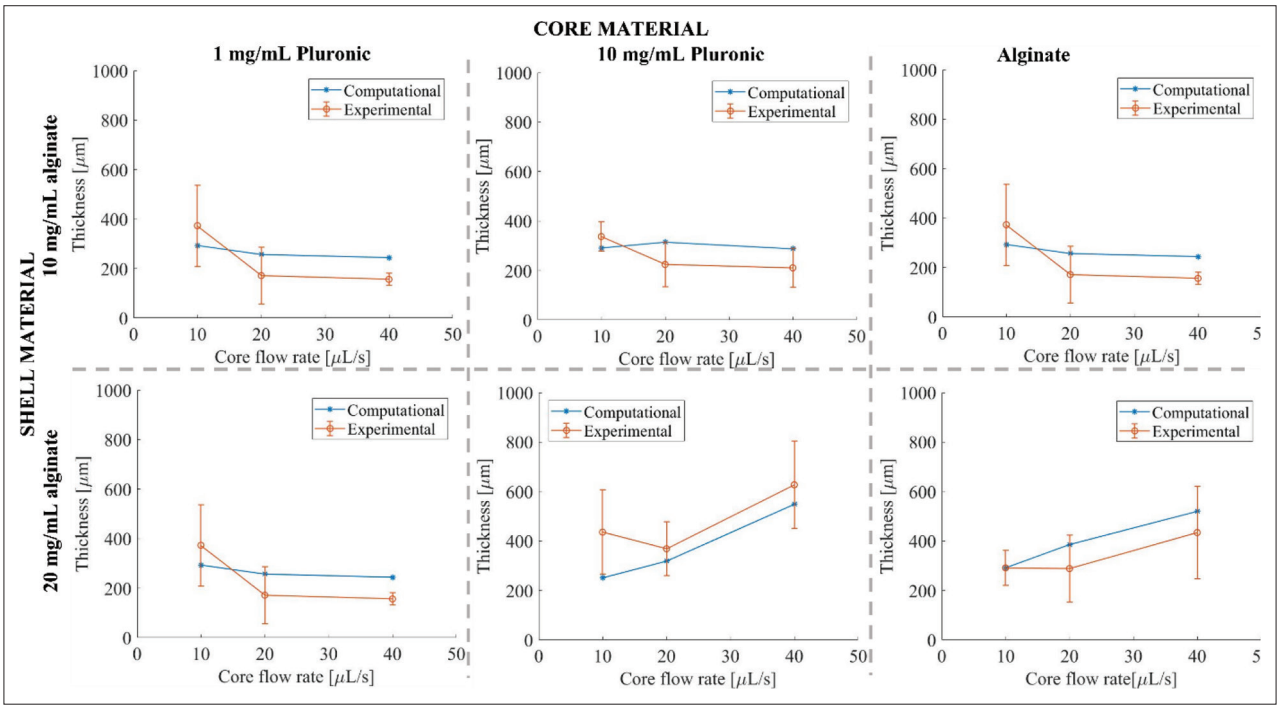

Figure S4. Comparison between the experimental (red line) and computational (abD_0, blue line) thickness values in different combination of core–shell materials as a function of the extrusion core flow rates, in the case of needle 1 ($p > 0.05$).

The time-dependent numerical study was performed on the final mesh structure. The method of lines was implemented in Comsol to solve the partial derivative equations (PDEs) related to space and time. In this method, space is discretized using the FEM, thus forming a system of ordinary differential equations (ODEs). Then, these ODEs are solved using the backward Euler method with a time step of 0.001 s.

S5. Computational and experimental dataset comparison

Figure S3 shows the comparison of experimental and computational results obtained with the modified diffusion coefficient with and without the Brinkmann coefficient. Data estimated using the abD_0 coefficient resulted more similar (*t*-test, $p < 0.05$) to the experimental ones with the $abD_{0.}$

Figures S4 and S5 show that experimental and computational thickness values are comparable in the different conditions investigated, thus validating the computational model using the novel definition of the diffusion coefficient. Statistical

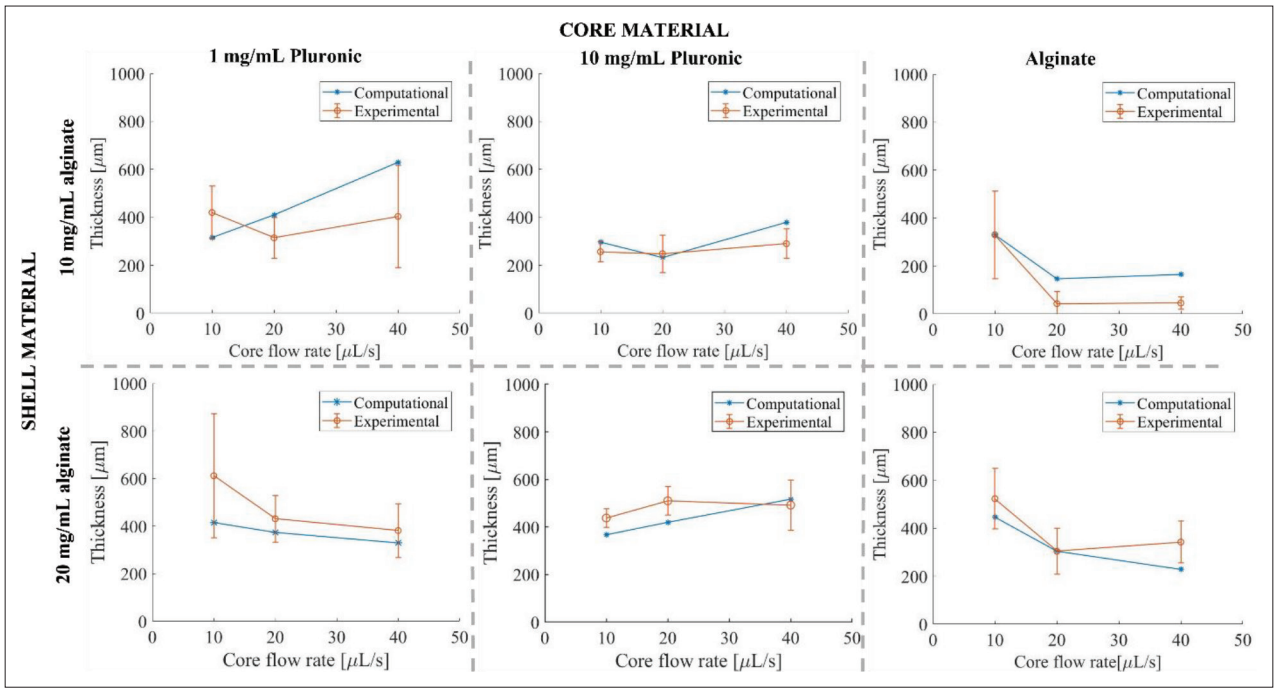

Figure S5. Comparison between the experimental (red line) and computational (abD_0, blue line) thickness values in different combination of core–shell materials as a function of the extrusion core flow rates, in the case of needle 2 ($p > 0.05$).

analysis (*t*-test) was performed, verifying that computational and experimental data were not significantly different ($p > 0.05$).

S6. Geometric features for the different extrusion conditions

Figures S6 and S7 show the geometric features of the core–shell structures (measured using image analysis as described in the main text) as a function of core extrusion flow rate in the different conditions investigated. These subgroups of the dataset were selected according to the core composition, which was suggested by the PCA as the parameter which most strongly influences droplets shape and size. The statistical analysis (*t*-test) carried out on these subgroups also highlights that other parameters such as flow rate also play a role (minor) in controlling the geometrical outcomes.

S7. External air flow

Air flow at 0, 0.5, and 1 bar was applied to the needle extremities through the air channels connected with a pressure regulator. As shown in Figure S8, the application of an external air flow resulted in a worsening of the core–shell structure and symmetry. Although an external air flow was used in the literature to modulate bead size and improve roundness, this parameter was not suitable for the fabrication of core–shell structures since it is likely accelerating the mixing of the different solution in the CSCs, greatly reducing core–shell distinction. Therefore, all core–shell structures were printed in the absence of air flow.

S8. Effect on Pluronic in the shell

The addition of Pluronic in the shell alginate solution resulted in a reduction of CSCs roundness (73.05% ± 8.42%) compared to the ones without Pluronic (97.3% ± 0.74%). This is probably because Pluronic reduces the air–material surface tension (Figure S9). Moreover, for the solid core, the use of Pluronic in the core did not significantly affect CSCs fabrication in terms of roundness.

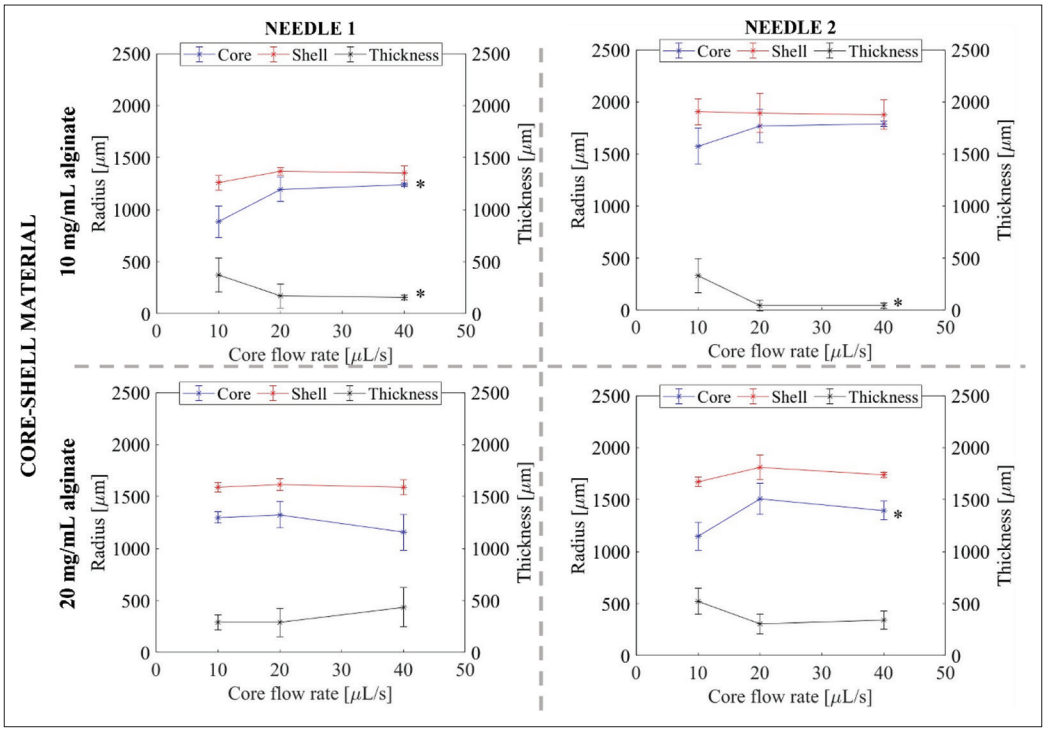

Figure S6. Core and shell radii and shell thickness trends as a function of the core flow rate, in the case of a solid core (* $p < 0.05$).

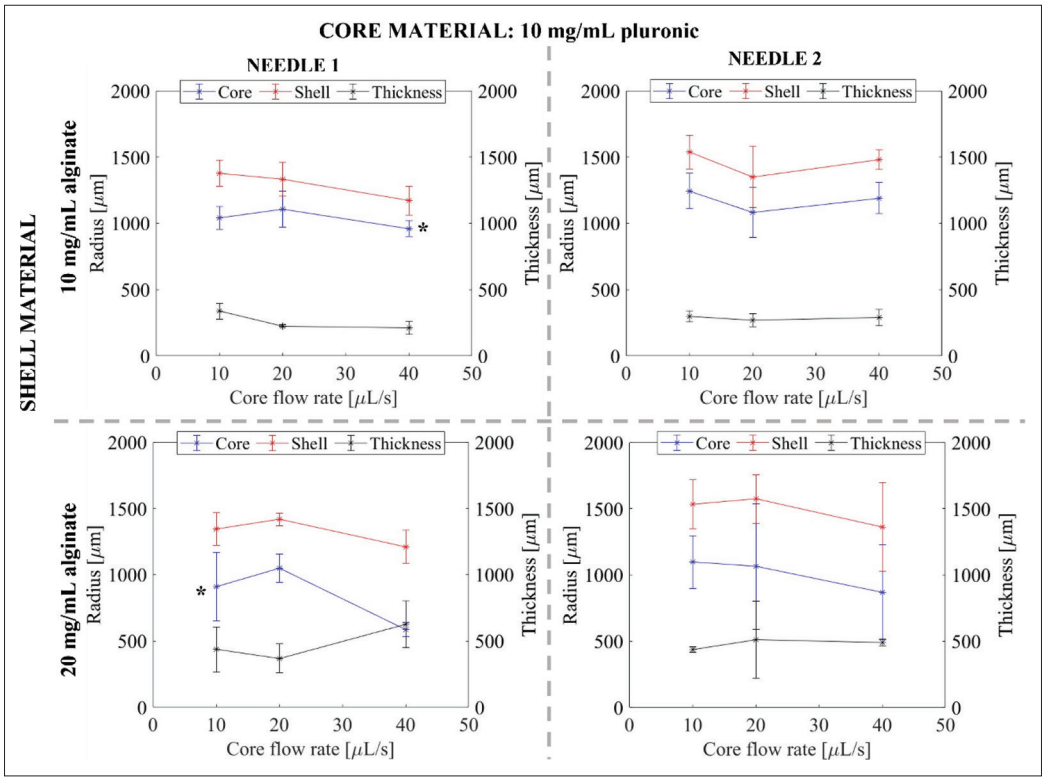

Figure S7. Core and shell radii and shell thickness trends as a function of the core flow rate, in the case of a liquid core (* $p < 0.05$).

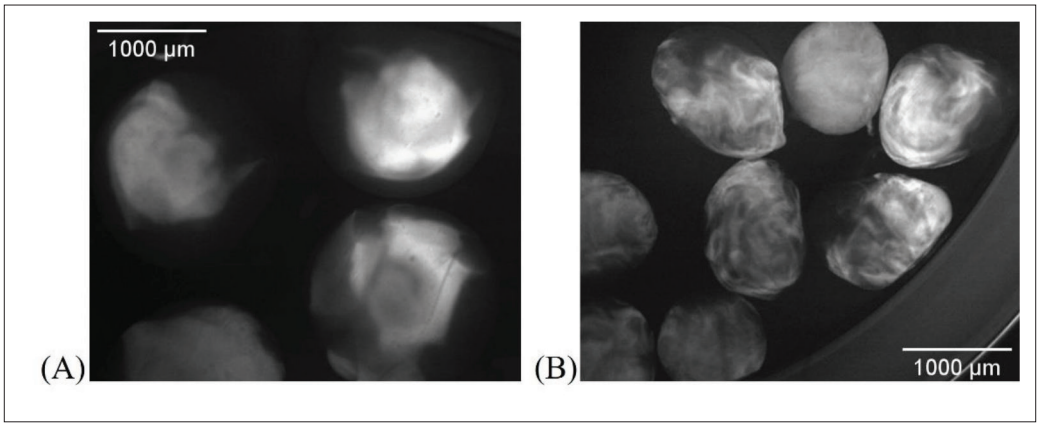

Figure S8. Core–shell structures fabricated using an external air flow with (A) 0.5 bar and (B) 1 bar.

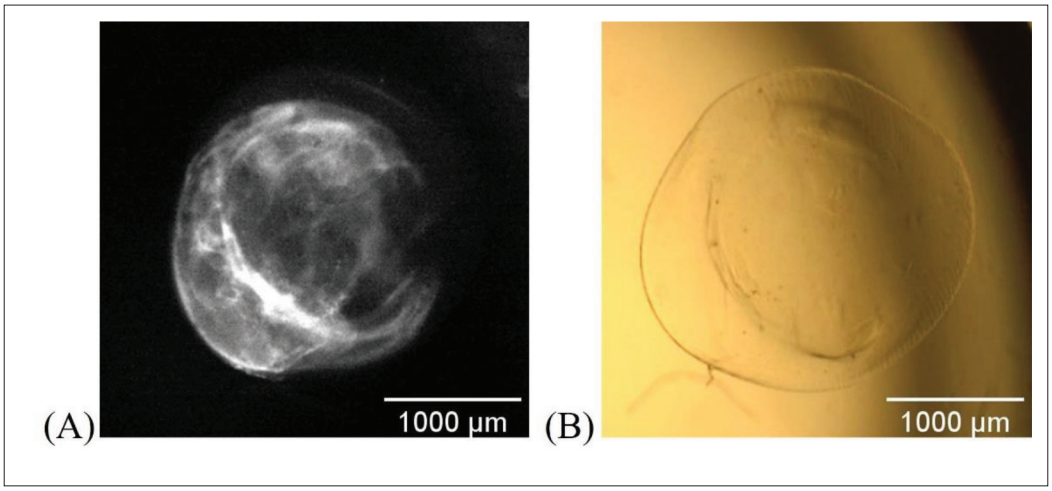

Figure S9. Core–shell structures composed of 10 mg/mL alginate and 1 mg/mL Pluronic in the shell and 10 mg/mL alginate in the core (core flow rate 10 µL/s, shell flow rate 40 µL/s, needle 1). (A) Image in brightfield; (B) image in epifluorescence.

S9. Alginate mechanical characterization

The alginate mechanical properties were investigated to identify the mechanical stimuli that the cells undergo in the core–shell constructs. In particular, the elastic modulus of alginate was derived from the slope of the stress–strain curves in the linear viscoelastic region[10]. Briefly, 10 and 20 mg/mL alginate hydrogels were prepared by crosslinking the alginate solutions in custom molds (13 mm diameter, 8 mm height) for 15 min with a 0.1 M $CaCl_2$ solution. The hydrogels were tested with unconfined bulk compression tests (0.01 s^{-1} strain rate), 20% linear viscoelastic region (LVR) using the Zwick/Roell ProLine Z005 uniaxial testing device (Germany). The measured apparent elastic modulus resulted in 4.11 ± 0.22 kPa for 10 mg/mL alginate hydrogels and 4.17 ± 0.36 kPa for 20 mg/mL alginate hydrogels.

S10. Estimation of Thiele's modulus in the core shell constructs

To verify that the CSCs were not oxygen-deprived, we generated a simple FEM model in 2D axial symmetry considering oxygen reaction and diffusion in spherical cell-laden gel. In correspondence with the experiments, we represented an inner domain with 5 million A549 cells/mL in a liquid core of radius R_c = 1000 mm and 6 million fibroblasts/mL in an alginate shell with outer radius R_s = 1500 mm. The single cell maximal oxygen consumption rate of A549 cells (OCR_{A549}) was estimated from Wu *et al.* (3.3×10^{-17} mol/cells)[11]; that of fibroblasts ($OCR_{CCD\text{-}18co}$) was estimated from Streeter and Cheema (1.19×10^{-17} mol/cells)[12]. The oxygen diffusion constant (D_0) in the liquid core was 3×10^{-9} m^2/s[13], while D_{app} in the alginate shell was estimated as described in section 2.1 considering an oxygen R_h derived from D_0 (Equation III in section 2.2).

In the worst case of zero-order oxygen consumption, the Thiele's modulus F^2 in the core (Equation S-VI)[13] and in the shell (Equation S-VII) is given by:

$$\Phi^2 = \frac{R_c^2 \rho_{A549} OCR_{A549}}{D_0 C_0} \quad \text{(S-VI)}$$

$$\Phi^2_{shell} = \frac{\left(R_s - R_c\right)^2 \rho_{CCD-18co} OCR_{CCD-18co}}{D_{app} C_0} \quad \text{(S-VII)}$$

Considering a boundary oxygen concentration C_0 = 0.21 mol/m^3 for the shell and C_0 = 0.17 mol/m^3 for the core (equal to C_0 at the core–shell interface, estimated from the FEM model), the average F^2 for CSC1 was equal to 0.31, while for CSC2, it was equal to 0.50. These values, which are < 1, imply that oxygen diffuses through the core–shell constructs at a faster rate than it is consumed, which might explain the high viability values observed in our experiments.

References

1. Ghauri SA, Ansari MS, 2012, Increase of water viscosity under the influence of magnetic field increase of water viscosity under the influence of magnetic field. *J Appl Phys,* 100(6), 066101: 100–102.
2. Vargaftik NB, Volkov BN, Voljak LD, 1983, International tables of the surface tension of water. *J Phys Chem Ref Data,* 12(3): 817–820.
3. Pluen A, Netti PA, Jain RK, *et al.*, 1999, Diffusion of macromolecules in agarose gels: Comparison of linear and globular configurations. *Biophys J,* 77(1): 542–552.
4. White JA, Deen WM, 2002, Agarose-dextran gels as synthetic analogs of glomerular basement membrane: Water permeability. *Biophys J,* 82(4): 2081–2089.
5. Zhong D, Huang X, Yang H, *et al.*, 2010, New insights into viscosity abnormality of sodium alginate aqueous solution. *Carbohydr Polym,* 81(4): 948–952.
6. Potter K, Balcom BJ, Carpenter, TA, *et al.*, 1994, The gelation of sodium alginate with calcium ions studied by magnetic resonance imaging (MRI). *Carbohydr Res,* 257(1): 117–126.
7. Bharatiya B, Ghosh G, Aswal VK, *et al.*, 2010, Effect of n-hexanol and n-hexylamine on the micellar solutions of pluronic F127 and P123 in water and 1M NaCl. *J Dispers Sci Technol,* 31(5): 660–667.
8. Hajikhani A, Scocozza F, Conti M, *et al.*, 2019, Experimental characterization and computational modeling of hydrogel cross-linking for bioprinting applications. *Int J Artif Organs,* 42(10): 548–557.
9. Hajikhani A, Scocozza F, Conti M, *et al.*, 2019, Experimental characterization and computational modeling of hydrogel cross-linking for bioprinting applications. *Int J Artif Organs,* 42: 548–557.
10. Cacopardo L, Guazzelli N, Ahluwalia A, 2022, Characterizing and engineering biomimetic materials for viscoelastic mechanotransduction studies. *Tissue Eng Part B Rev,* 28(4): 912–925.
11. Wu M, Neilson A, Swift AL, *et al.*, 2007, Multiparameter metabolic analysis reveals a close link between attenuated mitochondrial bioenergetic function and enhanced glycolysis dependency in human tumor cells. *Am J Physiol Cell Physiol,* 292(1): 125–136.
12. Streeter I, Cheema U, 2011, Oxygen consumption rate of cells in 3D culture: The use of experiment and simulation to measure kinetic parameters and optimise culture conditions. *Analyst,* 136(19): 4013–4019.
13. Magliaro C, Mattei G, Iacoangeli F, *et al.*, 2019, Oxygen consumption characteristics in 3D constructs depend on cell density. *Front Bioeng Biotechnol,* 7: 251.